Finite Element-Based Characterization of Pore-Scale Geometry and Its Impact on Fluid Flow

2 authors:

Lateef Akanji
University of Aberdeen
27 PUBLICATIONS   **131** CITATIONS

SEE PROFILE

Stephan K Matthai
University of Melbourne
134 PUBLICATIONS   **2,929** CITATIONS

SEE PROFILE

Some of the authors of this publication are also working on these related projects:

Still multiphase upscaling in naturally fractured reservoirs (1) and upscaling of saturation functions for CO2 injection in heterogeneous sandstones (2), fault stability analysis (3) View project

Pore scale fluid flow characterisation of shale rocks View project

Finite Element-Based Characterization of Pore-Scale Geometry and Its Impact on Fluid Flow

Lateef T. Akanji · Stephan K. Matthai

Abstract   We present a finite element (FEM) simulation method for pore geometry fluid flow. Within the pore space, we solve the single-phase Reynold's lubrication equation—a simplified form of the incompressible Navier–Stokes equation yielding the velocity field in a two-step solution approach. (1) Laplace's equation is solved with homogeneous boundary conditions and a right-hand source term, (2) pore pressure is computed, and the velocity field obtained for no slip conditions at the grain boundaries. From the computed velocity field, we estimate the effective permeability of porous media samples characterized by section micrographs or micro-CT scans. This two-step process is much simpler than solving the full Navier–Stokes equation and, therefore, provides the opportunity to study pore geometries with hundreds of thousands of pores in a computationally more cost effective manner than solving the full Navier–Stokes' equation. Given the realistic laminar flow field, dispersion in the medium can also be estimated. Our numerical model is verified with an analytical solution and validated on two 2D micro-CT scans from samples, the permeabilities, and porosities of which were pre-determined in laboratory experiments. Comparisons were also made with published experimental, approximate, and exact permeability data. With the future aim to simulate multiphase flow within the pore space, we also compute the radii and derive capillary pressure from the Young–Laplace's equation. This permits the determination of model parameters for the classical Brooks–Corey and van-Genuchten models, so that relative permeabilities can be estimated.

Keywords   Micro-CT scans · Thin section micrographs · Effective permeability · Pore-scale geometry · Finite element · Reynold's lubrication equation

L. T. Akanji (✉) · S. K. Matthai
Institute of Petroleum Studies, Department of Earth Science and Engineering,
Imperial College London, South Kensington Campus, London, SW72AZ, UK
e-mail: l.akanji06@ic.ac.uk

S. K. Matthai
e-mail: s.matthai@ic.ac.uk

🍦 Springer

List of Symbols

V	Volume (m^3)
F	Right-hand term
N	Interpolation function
R	Pore radius (m)
P	Pressure (Pa)
W	Weighting function
K	Permeability (m^2)
a	Pore diameter/channel width (m)
μ	Fluid viscosity (Pa s)
ψ	Parabolic function
θ	Rock-fluid contact angle
σ	Interfacial tension (N/m)
ρ	Fluid density (kg/m^3)
ϕ	Porosity
λ	Brooks–Corey parameter
γ	van-Genuchten parameter
ω	Domain boundary
$\hat{n}$	Unit normal to the boundary
ϵ	van-Genuchten parameter

Subscript

x, y	Directions
a	Pore diameter
nw	Non-wetting
w	Wetting
m	Mean
e	Effective

Superscript

A, B, and C	Relative permeability parameters
T	Matrix transpose
e	Element

1 Introduction

An understanding of flow processes in porous media is of great importance in many fields such as hydrology, nuclear waste disposal, and reservoir engineering. Macroscopic properties—effective permeability, capillary pressure, and relative permeability—are needed when modeling flow and transport at the continuum scale, be it transport of non-aqueous phase liquids (NAPL) in contaminant clean-up or the production of oil using reservoir water flooding.

However, these macroscopic properties are difficult to obtain. It is possible to conduct physical experiments on samples; however, experimental measurements of these constitutive relations are extremely difficult to perform, and at low saturation, the results are very uncertain (Honarpour et al. 1986; Dullien 1992). Hence, there is a need to develop models that can

predict fluid flow and transport properties directly from the geometry of the pore space in an accurate and computationally efficient manner.

Any theoretical or numerical approach to this problem not only needs a detailed understanding of the flow and transport behavior at the pore level (Blunt 2001) but also an accurate and realistic characterization of the structure of the porous medium (Pereira et al. 1996 and Valvatne and Blunt 2004). During the last two decades, our knowledge of the physics of two- and three-phase flow at the pore level has considerably increased through experimental investigation of displacements in core samples and micromodels (Adler et al. 1990; Soll et al. 1993; Øren and Pinczewski 1995) combined with pore-scale imaging of the flow (Wildenschild et al. 2005). In order to describe the geometry of the pore spaces, Adler et al. (1990), Roberts (1997), and Okabe and Blunt (2004) have developed statistical- and process-based (Øren and Bakke 2002) models. In addition, the pore space as well as the fluid distribution within it has been studied directly using micro-CT tomography (Dunsmuir et al. 1991; Spanne et al. 1994).

Figure 1 shows examples of three-dimensional micro-CT images of LV60- and Ottawa-sandstone samples (Talabi et al. 2008). It is possible to simulate multi-phase flow directly on a two- or three-dimensional pore-space images by solving the Navier–Stokes equations or by using the Lattice–Boltzman techniques (Grunau et al. 1993; Ferreol and Rothman 1995). However, the caveats in using these methods are considerable (Guo and Zhao 2002).

In this article, we present a computationally more effective, unstructured FEM-based discretization and simulation method for single-phase flow in porous media.

Following the description of our model, it is verified with the analytical solution to a simplified form of the Navier–Stokes equation, the Reynold's lubrication equation. The verified model is then validated on two micro-CT scans of porous media samples: (1) LV60 sandstone and (2) Ottawa sandstone. For both these, the permeability and porosity are known from laboratory experiments and can be compared with the model results. The single-phase flow experiments are followed by computations of the pore radius, capillary pressure, relative permeability, and saturation distributions within the pore geometry. All computations were carried out using Complex System Modeling Platform, CSMP++ (Matthai et al. 2004)—an object-oriented finite element-based package for modeling complex geological processes.
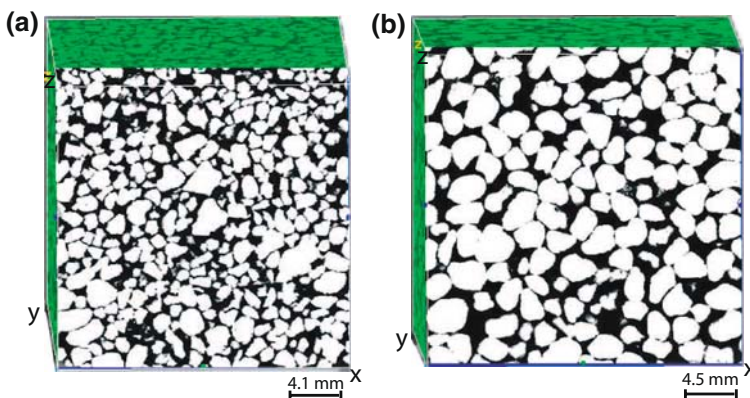

Fig. 1 3D micro-CT images of **a** LV60 sandstone and **b** Ottawa sandstone samples showing pore-space (*black*) and grains (*white*) (Talabi et al. 2008)

2 Pore-Scale Single-Phase Flow Formulation and Finite Element Model

The partial differential equations governing the flow of an incompressible Newtonian fluid are the Navier–Stokes equations

$$\rho \frac{\partial \mathbf{u}}{\partial t} = \mu \, \triangledown^2 \mathbf{u} - \rho(\mathbf{u} \cdot \triangledown)\mathbf{u} - \triangledown P, \tag{1}$$

and the law of mass conservation can be written as

$$\triangledown \cdot \mathbf{u} = 0. \tag{2}$$

The variables $\triangledown P$, ρ, μ, and $\mathbf{u}$ are the reduced pressure gradient, fluid density, fluid viscosity, and velocity vector, respectively. $\left(\frac{\partial}{\partial t}\right)$ is the "partial derivative" with respect to time. The boundary condition includes "no slip" at any boundary between the fluid and the solid; this implies that at the grain walls, not only is the normal component of the velocity equal to zero but also the tangential component vanishes as well. It is also assumed that the appreciable body force is taken to be that due to gravity. This is defined by the reduced pressure gradient (Batchelor 1967, p. 176; Phillips 1991, p. 26) $\triangledown P = \triangledown p + \rho g \mathbf{e}_v$, where p is the pressure and $\mathbf{e}_v$ is a unit vector in the vertical direction.

The compressibility effect is important for transient problems because it contributes to the storativity of the rock/fluid system. However, since the relationship between permeability and pore geometry is most readily studied using steady-state flow, we will ignore transient effects and assume that the fluid density is constant. This implies that at a fixed point in space, the velocity does not vary with time, and the equations reduce to

$$\mu \, \triangledown^2 \mathbf{u} - \rho(\mathbf{u} \cdot \triangledown)\mathbf{u} = \triangledown P. \tag{3}$$

The presence of the advective acceleration term generally causes the equations to be nonlinear, and consequently, very difficult to solve. When this term is far smaller than the viscous term, a typical situation in flows where the fluid velocities are very slow (creeping flow), the viscous forces are very large, or the length scales of the flow are very small, i.e., the Reynolds number is small, and the fluid is incompressible, we have the Stoke's equation. This condition is met in most flows in porous media. Excellent references on the subject are Happel and Brenner (1983), who also provide a historical perspective, and Pozrikidis (1992).

Here, we will evaluate whether this equation suffices for modeling single-phase flow in porous media. Dropping the advective acceleration term $\rho(\mathbf{u} \cdot \triangledown)\mathbf{u}$, we are left with the viscous term on the left-hand side of the equation:

$$\mu \, \triangledown^2 \mathbf{u} = \triangledown P. \tag{4}$$

This is Stoke's linear creeping flow equation. A special case of this equation where the pressure gradient is aligned with the direction of flow is the Reynold's lubrication equation and has been solved analytically (e.g., Zimmerman and Bodvarsson 1996) for the case of viscous fluid flow between two parallel plates (Fig. 2). The total volumetric flux through a channel can also be found by integrating the velocity across the geometry (Zimmerman and Bodvarsson 1996).

2.1 Numerical Solution Sequence

We solve Eq. 4 in two- and three-dimensional pore spaces numerically using a two-step process: We first solve for a function $\psi(x, y, z)$ and then compute the pressure gradient $\triangledown P$.
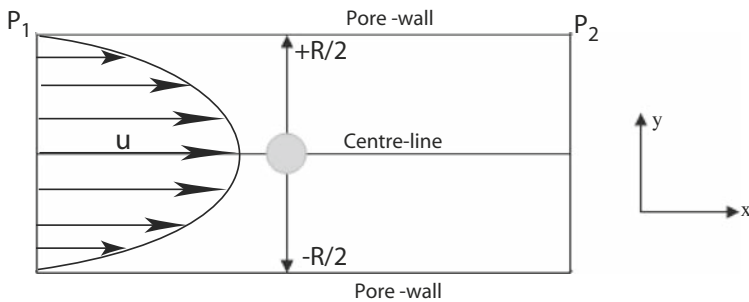
Fig. 2 Two-dimensional pore geometry showing assigned uniform pressures $P1$ and $P2$ on the left and right boundaries and a channel parabolic velocity profile

We assume that the pore space velocity equation can be written as

$$\mathbf{u} = \frac{\psi_k(x_k, y_k, z_k)}{\mu} \nabla P, \tag{5}$$

where $\psi_k(x_k, y_k, z_k)$ represents a twice-differentiable real-valued function of the coordinates x, y, and z defined on all the nodes $k = 1, 2, 3, \ldots, n$ that make up the FEMs. $\psi(x, y, z)$ is obtained after solving

$$\nabla^2 \psi(x, y, z) = 1, \tag{6}$$

with $\psi(x, y, z) = 0$ at the grain boundaries.

In order to compute the pressure field, we substitute Eq. 5 into Eq. 4, resulting in

$$\nabla^2 (\psi(x, y, z) \nabla P) = \nabla P, \tag{7}$$

which can also be written as

$$\psi(x, y, z) \nabla^3 P + \nabla \psi(x, y, z) \nabla^2 P + \nabla^2 \psi(x, y, z) \nabla P = \nabla P. \tag{8}$$

Assuming that the pressure variation within the pore space is only gradual, we ignore higher-order terms (3 and above) of the pressure derivatives. Substituting Eq. 6 in Eq. 8 gives

$$\nabla \psi(x, y, z) \nabla^2 P = 0, \tag{9}$$

which is solved for pressure.

In two-dimensional geometries, we simply reduce the coordinates to x and y. By solving Eq. 6 and then Eq. 9 for pressure using the computed function $\psi(x, y, z)$, we are able to compute piecewise constant velocity on each FEM in a very efficient manner.

2.2 FEM Discretization

In order to compute the velocity field on each finite element, we write the integral form of Eqs. 2 and 4 for an incompressible fluid over a typical element Ω^e bounded by Γ^e as

$$\int_{\Omega^e} W \frac{\partial \mathbf{u}_i}{\partial x_i} dx = 0 \tag{10}$$

$$\int_{\Omega^e} \frac{\partial w_i}{\partial x_i} \left[-P \delta_{ij} + \mu \left(\frac{\partial \mathbf{u}_i}{\partial \mathbf{x}_j} \right) \right] dx - \oint_{\Gamma^e} w_i \Upsilon_i ds = 0, \tag{11}$$

where the Eqs. 10 and 11 have been written for a Cartesian geometry in an Eulerian reference frame with the indices $i, j = 1, 2, 3$ (or $i, j = 1, 2$ for two-dimensional problems). w, W are weighting functions see Reddy and Gartling (2001) for further details and

$$\Upsilon = \left[\mu \left[(\nabla \mathbf{u}) + (\nabla \mathbf{u})^{\mathrm{T}} \right] - P \delta_{ij} \right] \cdot \mathbf{n}, \tag{12}$$

where $\mathbf{n}$ is the unit normal to the boundary. Using a linear finite element method with linear interpolation functions N_e, where the number of elements e $= 1,2,3,\ldots,m$, the pressure and velocity fields (P, $\mathbf{u}$) are approximated by expansions of the form:

$$\mathbf{u}(x) = \sum_{e=1}^{m} N_e \mathbf{u}_i(x) = \psi^{\mathrm{T}} \mathbf{u}_i \tag{13}$$

$$P(x) = \sum_{l=1}^{L} \chi_l(x) P_l = \psi^{\mathrm{T}} P, \tag{14}$$

where ψ is a column vector of the parabolic function, and $\mathbf{u}_i$ and P are vectors of nodal values of velocity components and pressure, respectively. In this Bubnov–Galerkin method, the weighting functions are taken as the same interpolation functions. Substitution of Eqs. 13 and 14 into Eqs. 10 and 11 while taking Eq. 12 into consideration, results in the following FEM integral equations:

$$-\left[\int_{\Omega^e} \psi \frac{\partial \psi^{\mathrm{T}}}{\partial x_i} \mathrm{d}x \right] \mathbf{u}_i = 0 \tag{15}$$

$$\left[\int_{\Omega^e} \mu \frac{\partial \psi}{\partial x_i} \frac{\partial \psi^{\mathrm{T}}}{\partial x_j} \mathrm{d}x \right] \mathbf{u}_i - \left[\int_{\Omega^e} \frac{\partial \psi}{\partial x_i} \psi^{\mathrm{T}} \mathrm{d}x \right] P = \oint_{\Gamma^e} \psi \Upsilon_i \mathrm{d}s, \tag{16}$$

where superscript $(\cdot)^{\mathrm{T}}$ denotes the transpose of the enclosed vector or matrix. The above equations can be written symbolically in matrix form as

$$-W^{\mathrm{T}} \mathbf{u} = 0 \tag{17}$$

$$[A]\{\mathbf{u}\} - W P = \{F\}. \tag{18}$$

For a range of FEM shapes, the interpolation functions are defined elsewhere (Reddy and Gartling 2001; Huyakorn and Pinder 1983; Paluszny et al. 2007).

3 Verification of the Numerical Model

We start with the description of how the cross-sectional pore-space models are generated using a finite element mesh discretization, and then we give a stepwise procedure of how we verify our numerical model.

3.1 Pore-Space Model Generation

We start by obtaining a photomicrograph or a micro-CT scan of a porous medium. The digitized binary representation of the pore geometry is then thresholded and differentiated into two discontigous domains "GRAINS" and "PORES" in a Computer-Aided Design (CAD)
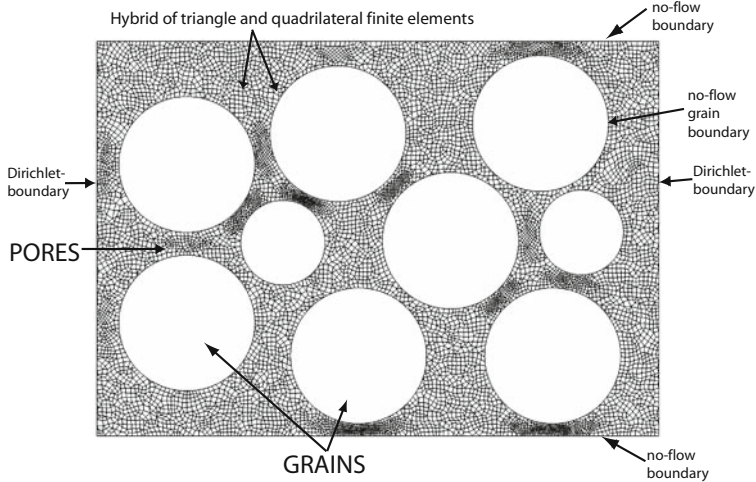
Fig. 3 Adaptively refined hybrid element mesh of an idealized 2D pore space consisting of *triangles* and *quadrilaterals*

geometrical package using a Boundary Representation (BREP) accomplished with Non-uniform Rational B-spline (NURBS) curves and surfaces. Interconnected pores are resolved into surfaces with four (in 2D) or six (in 3D) side boundaries for further import to the geometry editor of the mesh generation code. An unstructured FEM mesh with adaptive refinement at the constricted pore throats is generated by using hybrids of triangle and quadrilateral elements for 2D geometry (Fig. 3) or tetrahedra and hexahedra for 3D geometry. Third-order splines are used to represent grains and outer no-flow boundaries.

3.2 Model Setup and Computational Procedure

For single-phase flow, the flow models are designed with gaps at the in- and outflow boundaries (Fig. 3) to allow the assigned pressure to be uniformly distributed at these boundaries. An initial pressure which is greater than the capillary entry pressure of the largest pores is then assigned on the inflow boundary of the model for the fluid to percolate through. Only interconnected pore spaces are considered. The porosity, pore radius, pore velocity, and effective permeability within the model are computed in a stepwise manner. Oil saturation, capillary pressure, and relative permeabilities are derived later using these results.

Step 1 Porosity

The porosity is established as a by-product of the discretization of the pore-space and is computed using the following relations: Porosity = Pore Volume (V_p)/Bulk Volume (V_b), where V_b = (Grain Volume + Pore Volume), i.e.,

$$\phi = V_p / V_b. \tag{19}$$

Step 2 Pore-radius computation

Having solved Eq. 6 for ψ, we estimate the pore radius, r, by computing the magnitude of the derivative of this function. Figure 4a is a plot of the function $f(x, y)$, the gradient of which gives a symmetric distance from the peak (corresponding to the local minima within the
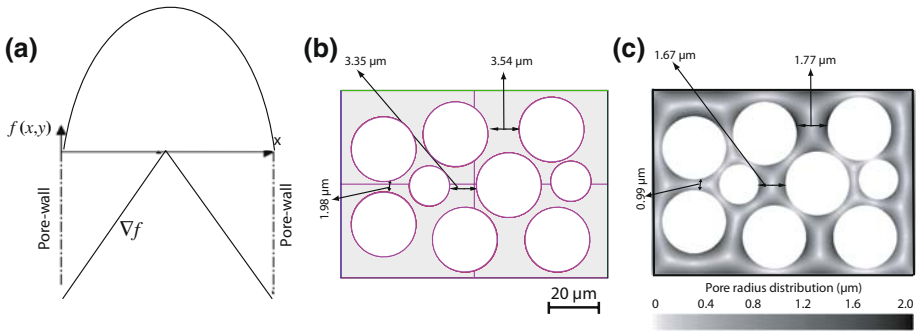
Fig. 4 **a** Determination of pore radius from the gradient of the parabolic function $f(x, y)$. **b** A simple 20×15 micron geometrical model from a CAD tool showing some pore diameter values. **c** CSMP++ *gray-scale* output showing computed pore radius distribution. The computed pore radii increase from the center to the grain boundaries. Typical pore-radii computations are shown with the *arrows* giving approximately the same values from the CAD measurement as those from the numerical model

pore-space) to the pore wall (corresponding to the grain boundary)—this is the pore-radius. In three-dimensional geometry,

$$r \Rightarrow |\nabla \psi(x, y, z)|. \tag{20}$$

A simple geometrical model (Fig. 4b) suffices to illustrate that the absolute value of this derivative is equal to the pore radius (Fig. 4c).

Step 3 Pore velocity

In order to verify the FEM approach and determine the minimum resolution required to obtain realistic parabolic velocity profiles, three numerical experiments were carried out using a simple $30 \times 20\,\mu$m channel flow model with channel widths $a = 6, 10$ and $16\,\mu$m, respectively (Fig. 5). A pressure gradient of $9,806\,\text{Pa}\,\text{m}^{-1}$ was assigned to allow the fluid to percolate through the channel. Regardless of whatever the width is, there will always be flow; hence, the focus of this sensitivity is to determine the minimum number of FEM required to replicate the analytically derived flow profile rather than channel width. An adequate resolution can be achieved based on how well the numerical flow velocity profile matches the analytical solution. In the three cases investigated here, 7, 14, and 21 FEMs span the reference slit. The velocity field obtained for each discretization is displayed in the figure. Since the computed velocities using a linear FEM are piecewise constant within each finite element, they show a stair-step parabolic profile in contrast to the smooth analytical solution. Figure 6 shows the velocity distribution within the pore of an idealized model shown in Fig. 4b.

A summary of the result for the sensitivity of velocity and flux estimate and their deviation from the theoretical solution for the three scenarios is given in Table 1.

We compare the computational efficiency of this approach with the reported study of Nunez et al. (2005), in which they solved the full Navier–Stokes equations. They used two parameters to quantify the computational efficiency of their method: (1) speed up $\text{Sp} = \text{Res-}$ olution time with 1 processor/Resolution time with p processors and (2) efficiency $= \text{Sp}/\text{p}$. Using the geometry shown in Fig. 3 with 553,763 elements which is more than double their 513×513 geometry (263,169 elements), we have Sp of 1.96 and efficiency of 0.98 for two processors while they had $\text{Sp} = 1.79$ and efficiency of 0.90 for two processors. This gives a significant computational efficiency with the potential to handle pore geometries with hundreds of thousands of pores in an efficient manner.
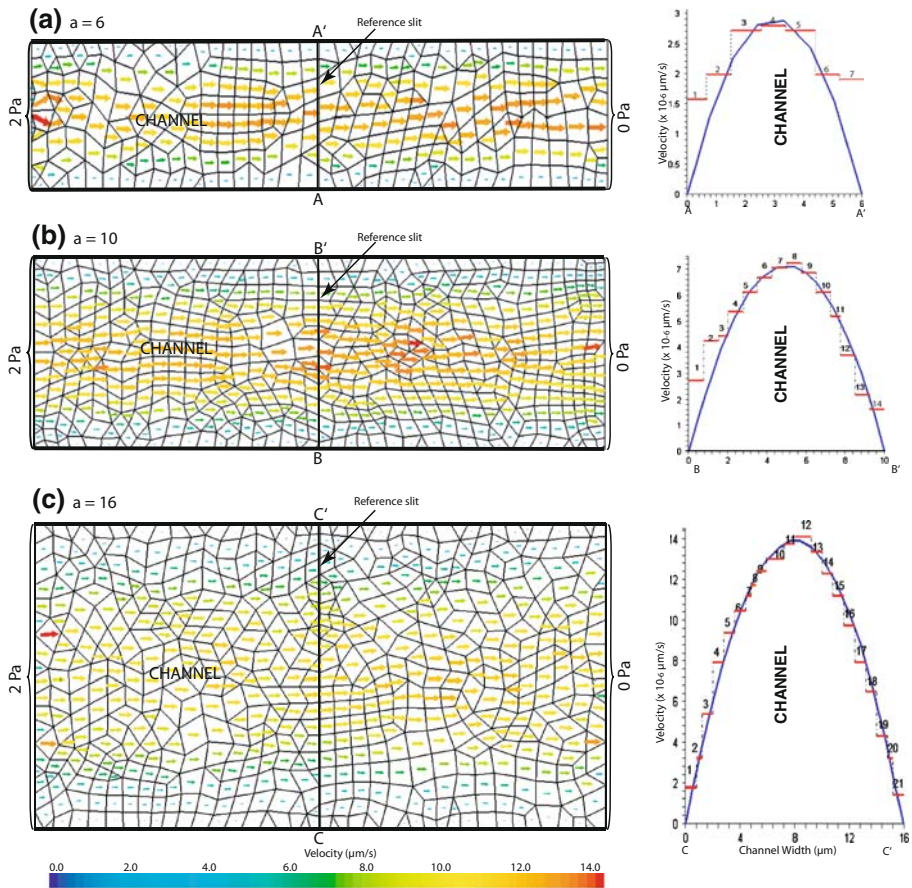
Fig. 5 Mesh sensitivity of channel model to know the number of FEM required to capture the full parabolic profile of the Reynold's lubrication equation: **a**–**c**—Matrix-channel model for the placement of 7, 14, and 21 FEM, respectively across a slit, and the velocity profile within the channel. The velocities are piecewise constant (*red*) within each FEM for the numerical computation and continuous (*blue*) for the analytical solution

Also, since dispersion is driven by the mean flow, we expect the dispersion coefficients D to be related to the characteristic length L, and mean flow velocity u by the expression $D = gLu$, where g is a geometric factor of the order of unity, L may depend on the structure of the porous medium direction relative to mean flow, flow field, and the interaction between molecular diffusion and convection (Sahimi et al. 1986). From the pore velocity fields computed, we can therefore measure dispersion coefficients in the porous medium. This will be discussed elsewhere.

Step 4 Single-phase effective permeability computation

Effective permeability—which can be used interchangeably with absolute permeability in single-phase experiments—is a measure of the ease with which a particular fluid can flow through a porous media. Having computed the velocity fields as described in Step 3, the effective permeability is computed by carrying out a single-phase numerical experiment;
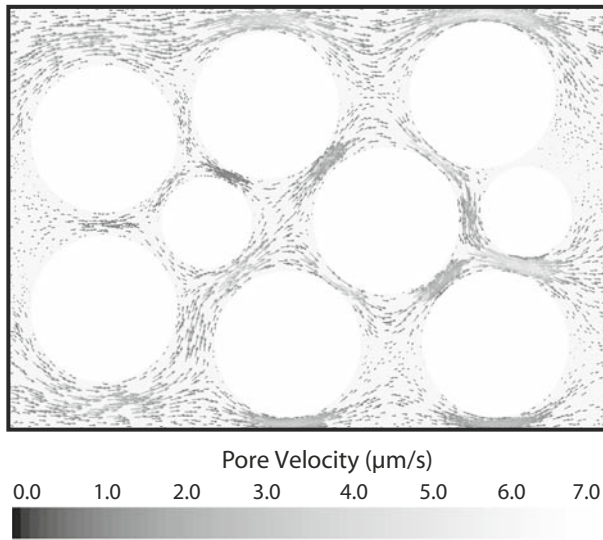
Pore Velocity (μm/s)

0.0   1.0   2.0   3.0   4.0   5.0   6.0   7.0

Fig. 6 Pore velocity distribution computed on the model shown in Fig. 4b

Table 1 Sensitivity of flux estimate on channel refinement

Case	a	b	c
Number of elements in channel	7	14	21
Max. deviation of channel velocity			
Mismatch between numerical and analytical solutions (%)	22.62	2.54	0.92
Integrated volume flux			
Mismatch between numerical and analytical solutions (%)	22.80	13.64	2.0

thus,

$$k_{\text{eff}} = \frac{q\mu}{A\,\triangledown\,P},\qquad(21)$$

where A is the cross-sectional area open to flow and q is the cross-sectional flux. We measure flux using a complementary finite volume discretization (cf. Paluszny et al. 2007).

3.3 Model Validation

The model was validated with three porous media samples: (1) 4.5×4.5 mm micro-CT scan of Ottawa sandstone, (2) 4.1×4.1 mm micro-CT scan of an LV60 sandstone both with predetermined porosity and permeability (Figs. 7a, b), and (3) a $600 \times 440\,\mu$m photo-micrograph of carbonate sand from Sombrero Beach, Marathon, Florida Keys, USA (Fig. 7c). In order to extract the pore geometry, the three images were thresholded in CAD and then meshed for simulation with the CSMP++ simulator.

Comparisons were also made with experimental, approximate, and exact permeability data reported by Zimmerman and Kumar (1991), in which they modeled permeability using
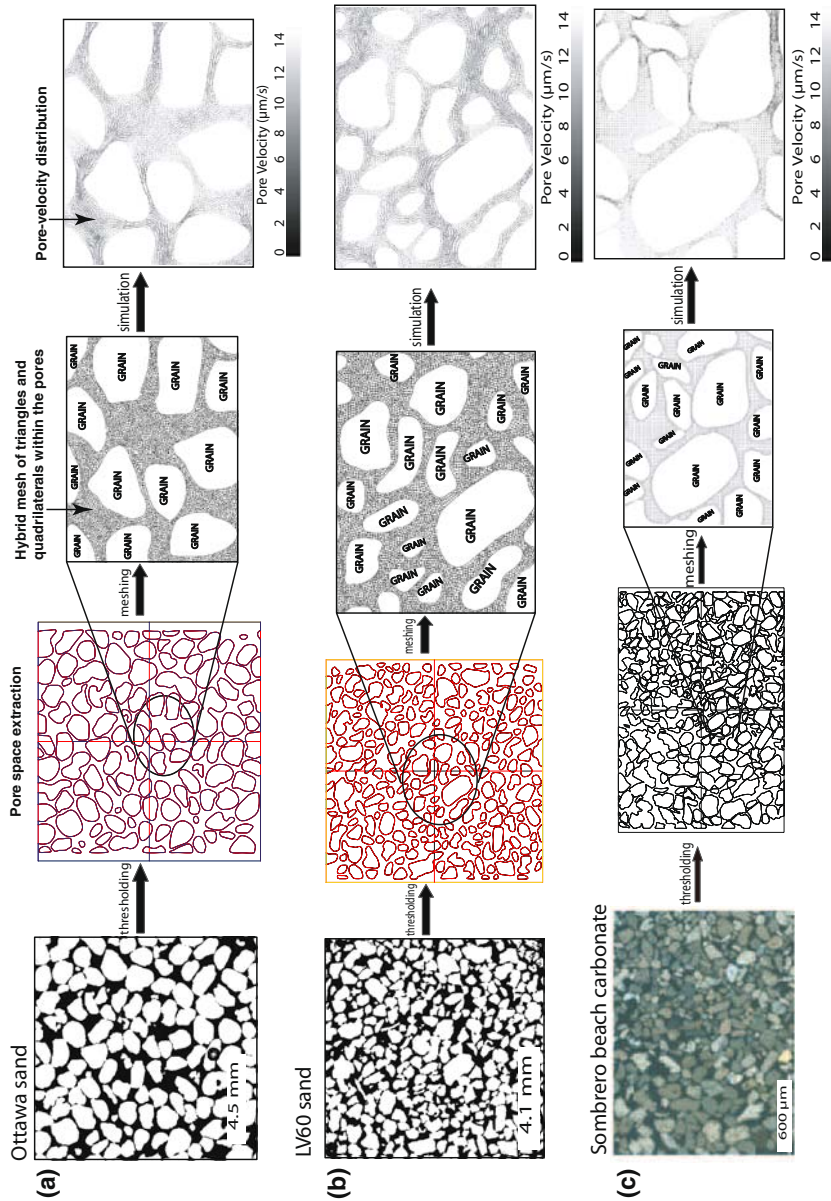
Fig. 7 a–c From left to right: Micro-CT scan of Ottawa, LV60 sandstone samples showing pores (*black*) and grains (*white*), and photomicrograph of Sombrero beach carbonate sandstone showing pores (*black*) and grains (*gray*); CAD representation of the pores and grains; hybrid mesh; and pore-velocity distributions within the pore space

Table 2 Summary of the comparison of computed versus the measured permeability of (i) Ottawa sandstone (ii) LV60, and (iii) Sombrero beach carbonate sandstone

Sample	Dimension (mm)	Porosity (%)	Permeability (D)
(1) Ottawa Sand			
Laboratory experiment	$4.5 \times 4.5 \times 4.5$	37	36
2D Numerical simulation	4.5×4.5	39	31
(2) LV60 sand			
Laboratory experiment	$4.1 \times 4.1 \times 4.1$	38	34
2D Numerical simulation	4.1×4.1	40	29
(3) Sombrero beach carbonate sand			
Laboratory experiment	–	–	–
2D Numerical simulation	0.6×0.44	36	28

cylindrical posts at a spatial density c, and post height-to-radius ratio, h/R. In order to validate our numerically computed permeability against their reported experimental data, we investigated seven (7) geometric models (inset Fig. 8) with the h/R in the range 0–3, but fixed c, of 0.09.

3.3.1 Pore Velocity

Pore velocity profiles for the three samples are also shown in Fig. 7, with the highest fluid velocity in the smallest pores.

3.3.2 Permeability and Porosity

Table 2 contains the computed permeability and porosity values and the results from the laboratory experiments for Ottawa and LV60 sandstone samples (Talabi et al. 2008). While the numerical computation is based on 2D cross sections only, the comparison between the two results is acceptable. There is no laboratory data for the Sombrero beach carbonate sandstone.

The data in Fig. 8 were extracted from Zimmerman and Kumar (1991). Yen and Fung (1973) experimental results for parallel-plate and cylindrical-post geometry with h/R in the range 3–10 are plotted and Lee (1969) data corresponding to the numerical solution of the full Navier–Stokes equations are shown. These results compare very well with two- and three-dimensional experimental data obtained with our method. Tsay and Wienbaum (1991) exact results do not match the experimental results as well as Lee's; however, the two points representing their exact results are very close to Zimmerman and Kumar (1991). The approximate expression of Lee provides a poorer fit.

Our 3D simulation model closely matches one of the two exact results of Tsay and Wienbaum (1991), as well as the Zimmerman and Kumar (1991) result. Within the range of investigation, the agreement between the experimental data of Yen and Fung (1973) and this model is fair.

3.4 Two-Phase Flow Properties

In this section, we investigate the pore-scale capillarity and relative permeability of porous media.
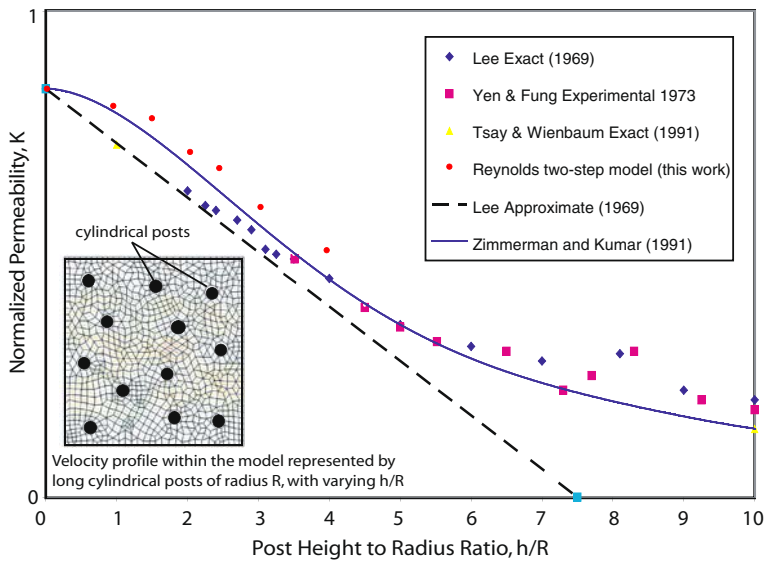
Fig. 8 Comparison of the permeability values measured by Yen and Fung (1973) with those predicted by this numerical method and by Zimmerman and Kumar (1991), Lee (1969), and Tsay and Wienbaum (1991). The areal concentration of posts, c, was held fixed at 0.09, while the ratio h/R was varied for seven (7) geometric models

3.4.1 Capillary Pressure, Pc (r)

When two immiscible fluids are in contact, a discontinuity in pressure exists between the two fluids and manifests itself in the curvature of the interface separating the fluids. This pressure difference, called the capillary pressure, is given by Laplace's equation (Collins and Cooke 1959):

$$Pc = \sigma_{12}(1/R_1 + 1/R_2), \tag{22}$$

where R_1 and R_2 are the principal radii of curvature of the interface, and σ_{12} is the specific energy of the interface or interfacial tension. It is customary to introduce the mean radius of curvature r_m (Dullien 1992) defined by

$$1/r_m = 1/2[(1/R_1) + (1/R_2)]. \tag{23}$$

Hence, Laplace's equation becomes,

$$Pc = Pnw - Pw = (2\sigma_{12}\cos\theta)/r_m. \tag{24}$$

The interface of the two immiscible fluids with the solid surface is at an angle termed the contact angle θ. This angle is determined by Young's equation (Collins and Cooke 1959):

$$\cos\theta = (\sigma_{s1} - \sigma_{s2})/\sigma_{12}, \tag{25}$$

where σ_{s1} is the specific-free energy (or interfacial tension) between the solid and fluid phase 1, and σ_{s1} is the corresponding quantity for the interface between the solid and the fluid phase 2.

Fig. 9 Capillary pressure
distribution and the spherical
bubble concept applied to the
model from Fig. 4b: The *gray
scale shading* illustrates the
internal pressure of a non-wetting
phase bubble placed in the
specific location

20 µm

Capillary Pressure (MPa)

0.5   10   20   30   40   50   60
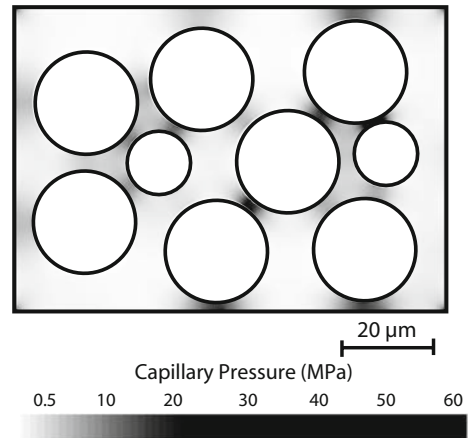
3.4.2 Capillary Pressure and the Spherical Bubble Concept

We assume that the non-wetting phase capillary pressure in a particular pore is equivalent
to the pressure a spherical bubble would experience when placed into that pore. This radius-
based concept is executed in Fig. 9. The black color indicates a high capillary pressure which a
spherical bubble placed within these pores would experience, while the white color indicates
a lower capillary pressure. This calculation is based on the pore radius which was computed
earlier from the derivative of the function ψ.

3.4.3 Relative Permeability Functions

With the knowledge of the pore-scale capillary pressure, we can now compute the relative
permeabilities of the wetting and non-wetting phases at capillary equilibrium as a function of
saturation. This approach is based on its fundamental definition on the micro-scale (Helmig
1997), where the capillary pressure is integrated over all the pores which are filled with a
particular phase.

$$K_{rw} = S_e^A \left[\frac{\int_0^S 1/[Pc(S*)]^B \, dS}{\int_0^1 1/[Pc(S*)]^B dS} \right]^C \tag{26}$$

$$K_{rnw} = (1 - S_e^A) \left[\frac{\int_S^1 1/[Pc(S*)]^B dS}{\int_0^1 1/[Pc(S*)]^B dS} \right]^C \tag{27}$$

$$S_e = (S_w - S_{wr})/(1 - S_{wr}). \tag{28}$$

The Brooks and Corey (1964) equations were derived in conjunction with the Burdine
theorem

$$K_{rw} = S_e^{\frac{2+3\lambda}{\lambda}} \tag{29}$$

$$K_{rnw} = (1 - S_e^2) \left(1 - S_e^{\frac{2+\lambda}{\lambda}} \right), \tag{30}$$

where λ is related to the pore size distribution of the material. Typical value of λ ranges from
0.2 to 3. Small λ values describe single grain size geometry, while large λ values indicate
highly non-uniform geometry.

	A	B	C
Table 3 Definition of the relative permeability parameters A–C			
Burdine (1953)	2	2	1
Mualem (1976)	0.5	1	2

The van-Genuchten (1980) model can also be parameterized using the approach of Mualem

$$K_{\text{rw}} = S_{\text{e}}^{\epsilon} \left[1 - (1 - S_{\text{e}}^{1/m})^m \right]^2 \tag{31}$$

$$K_{\text{rnw}} = (1 - S_{\text{e}})^{\gamma} \left(1 - S_{\text{e}}^{1/m} \right)^{2m}, \tag{32}$$

where $Pc(S*)$ represents the scaled capillary pressure curve. A, B, and C are defined in Table 3. The integration limits of the denominators are set to reflect that the non-wetting phase fills the larger pores and the wetting phase the smaller ones.

3.5 Pore-Radius and Capillary Pressure Distribution

The pore radius and capillary pressure distributions for Ottawa sandstone, LV60 sandstone, and Sombrero beach carbonate sandstone are shown in Fig. 10. Pores with the smallest radii have the highest capillary pressures, while the bigger pores have smaller capillary pressures, i.e., the inverse functional relation given by Laplace. The spherical bubble concept earlier discussed in Sect. 3.4.2 adequately describes the capillary pressure distribution within their pore geometry. Figure 10 is a graphical comparison between the pore radius distribution from the numerical result and the laboratory experimental result for Ottawa and LV60 sandstone samples. The pore radius versus capillary pressure distribution for Sombrero beach sandstone is represented by a barchart.

3.6 Oil Saturation Distribution

The non-wetting phase (oil) saturation distribution for the three porous media samples for different assigned non-wetting phase pressure values is also shown in Fig. 10. The non-wetting phase is set to only invade pores in which the capillary entry pressure is less than the assigned pressure. As the assigned pressure increases, the smaller pores are invaded. For the Sombrero beach carbonate sandstone, oil invades virtually all the pores at a pressure of about 40 MPa, whereas for Ottawa and LV60 samples, this occurs at low pressures of 5 and 8 MPa, respectively.

3.7 Capillary Pressure and Relative Permeability Curves

In order to derive the capillary pressure curve for Sombrero beach carbonate sandstone, we integrate the non-wetting phase saturation within the pore space at every assigned non-wetting phase pressure which is just equal to the computed capillary pressure (Sect. 3) and then generate plots as shown in Fig. 11a. The capillary pressure curve gives some information about the distribution of small and large pores within the model geometry. Most pores are large, but there is a significant fraction of small ones. The dominant effect of the smaller
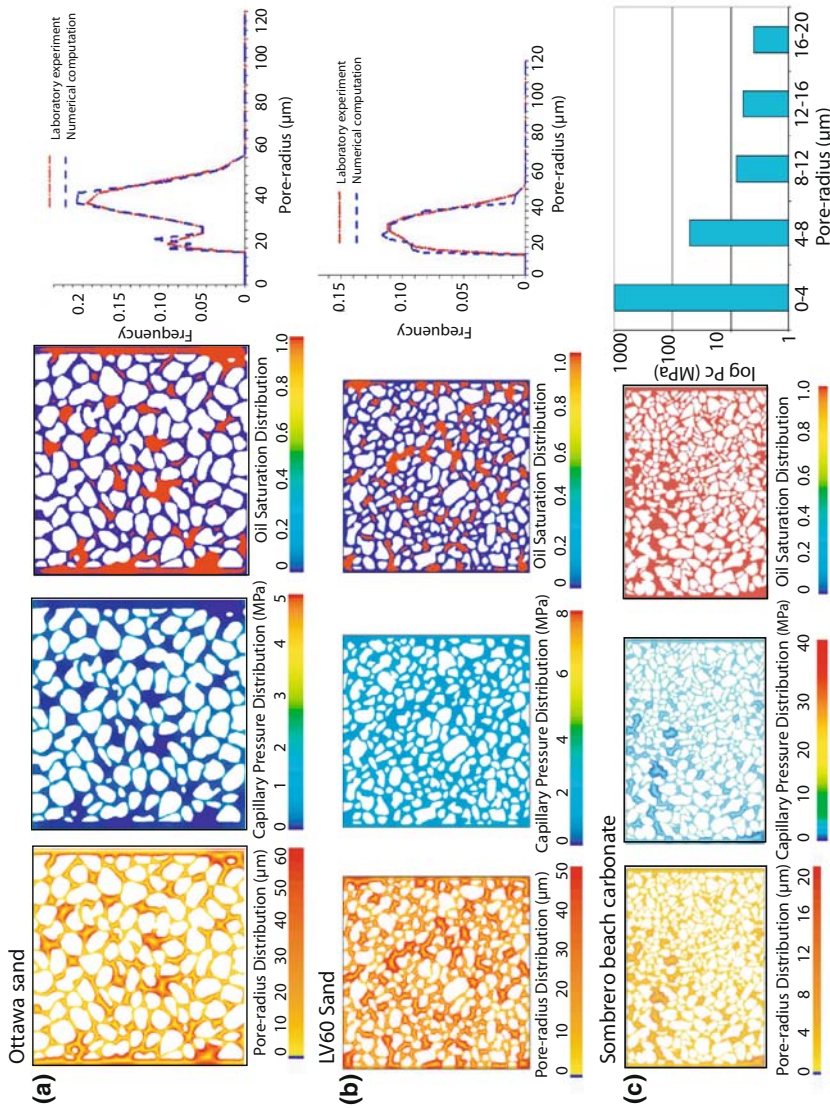
Fig. 10 **a–c** From left to right: pore radius distribution, *red color* indicates high pore radius; capillary pressure distribution, *light green* indicates high *P c*; oil saturation distribution at an assigned pressure of 2, 3, and 30 MPa for Ottawa sandstone, LV60 sandstone, and Sombrero beach carbonate, respectively; and *graphs* of pore radius distribution
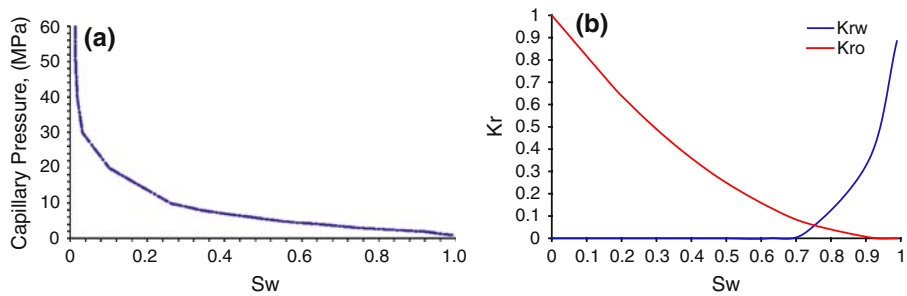
Fig. 11 **a** Capillary pressure curve and **b** relative permeability curves inferred for Sombrero beach carbonate sandstone

pores is shown by the sharp gradient between 0 and 0.25 water saturations, while the effect of the interconnectedness of the pores is shown by the negligibly small irreducible water saturation where the capillary pressure curve goes to infinity. Using Eqs. 30 and 31 with $\lambda = 2.5$, which signifies highly non-uniform pore size distribution (Fig. 10c), we infer the relative permeability curves for the sample as shown in Fig. 11b. These relative permeability curves show a typical strongly water wet behavior with a skewed cross-over at about 0.7.

4 Conclusions

A first principle-based approach of characterizing pore-scale geometry and describing the flow behavior within them was presented. We used a computationally cost effective two-step approach to solve the Reynold's lubrication equation in the pore space of a porous medium. This method has the potential to handle porous media samples with hundreds of thousands of pores which would be computationally prohibitive for the full Navier–Stoke's equation. This approach was verified against an analytical solution for a simple geometry, and the verified model was validated with two micro-CT scan data for which permeabilities and porosities were pre-determined in the laboratory experiments. The numerically computed permeabilities compare favorably with those obtained in the laboratory. Comparisons were also made with published experimental, approximate, and exact permeability data. Since our method also reveals the flow velocity spectrum in the pore space, it can also be used to measure dispersion coefficients. Simulations were carried out on the micro-CT scan and photomicrographic samples of selected porous media samples to derive the constitutive relationships governing single- and multi-phase flow. In order to accurately model fluid flow in porous media, the capillary, relative permeabilities, and saturation distribution can also be adequately captured by our method's extension to two-phase flow.

References

Adler, P.M., Jacquin, C.G., Quiblier, J.A.: Flow in simulated porous media. Int. J. Multiph. Flow **16**(4), 691–712 (1990)

Batchelor, G.K.: An Introduction to Fluid Dynamics. Cambridge University Press, New York (1967)

Blunt, M.J.: Flow in porous media—pore-network models and multiphase flow. Curr. Opin. Colloid Interface Sci. **6**, 197–207 (2001)

Brooks, R.H., Corey, A.T.: Hydraulic Properties of Porous Media. Hydrology Paper 3. Civil Engineering Department, University of Colorado, Boulder, CO (1964)

Burdine, N.T.: Relative permeability calculations from pore-size distribution data. Technical Report, Petroleum Transactions, AIME, pp. 71–78 (1953)

Collins, R.E., Cooke, C.E.: Fundamental basis for the contact angle and capillary pressure. Trans. Faraday Soc. **55**, 1602–1606 (1959)

Dullien, F.A.L.: Porous Media—Fluid Transport and Pore Structure. Academy Press, New York (1992)

Dunsmuir, J.H., Ferguson, S.R., D'Amico, K.L.: Design and operation of an imaging X-ray detector for microtomography. IOP Conf. Ser. **121**, 257–267 (1991)

Ferreol, B., Rothman, D.H.: Lattice-Boltzmann simulations of flow through Fontainebleau porous media. Transp. Porous Media **20**(1–2), 3–20 (1995)

Grunau, D., Chen, S., Eggert, K.: A Lattice Boltzmann model for multiphase fluid flows. Phys. Fluids A **5**(10), 2557–2562 (1993)

Guo, Z., Zhao, T.S.: Lattice Boltzmann model for incompressible flows through porous media. Phys. Rev. E **66**, 036–304 (2002)

Happel, J., Brenner, H.: Low-Reynolds Number Hydrodynamics. Kluwer, Boston (1983)

Helmig, R.: Multiphase Flow and Transport Processes in the Subsurface: A Contribution to the Modeling of Hydrosystems. Springer, Berlin (1997)

Honarpour, M., Koederitz, L., Harvey, A.H.: Relative Permeability of Petroleum Reservoirs, 1st edn. CRC Press, Boca Raton, FL (1986)

Huyakorn, P.S., Pinder, G.F.: Computational Methods in Subsurface Flow, pp. 25–53. Academic Press Inc., Orlando, FL (1983)

Lee, J.S.: Slow viscous flow in a lung alveoli model. Journal of Biomechanics **2**, 187–198 (1969)

Matthai, S.K., Geiger, S., Roberts, S.G.: Complex Systems Modeling Platform (CSMP5.0). User's Guide (2004)

Mualem, Y.: A new model for predicting the hydraulic conductivity of unsaturated porous media. Water Resour. Res. **12**, 513–522 (1976)

Nunez, I.I.A., Canalejo, M.C.C., Soto, J.L.C., Cara, E.F., Sanchez, J.R.G., Beltran, M.M.: Time and space parallelization of the Navier–Stokes equations. Comput. Appl. Math. **24**(3), 417–438 (2005)

Okabe, H., Blunt, M.J.: Prediction of permeability for porous media reconstructed using multiple-point statistics. Phys. Rev. E **70**, 066135 (2004)

⊘ren, P.E., Bakke, S.: Process based reconstruction of sandstones and prediction of transport properties. Transp. Porous Media **46**(2–3), 311–343 (2002)

⊘ren, P.E., Pinczewski, W.V.: Fluid distribution and pore-scale displacement mechanisms in drainage dominated three-phase flow. Transp. Porous Media **20**(1–2), 105–133 (1995)

Paluszny, A., Matthai, S.K., Hohmeyer, M.: Hybrid finite element-finite volume discretization of complex geologic structures and a new simulation workflow demonstrated on fractured rocks. Geofluids **7**(2), 186–208 (2007)

Pereira, G.G., Pinczewski, W.V., Chan, D.Y.C., Paterson, L., ⊘ren, P.E.: Pore-scale network model for drainage-dominated three-phase flow in porous media. Transp. Porous Media **24**(2), 167–201 (1996)

Phillips, O.M.: Flow and Reaction in Permeable Rocks. Cambridge University Press, Cambridge, UK (1991)

Pozrikidis, C.: Boundary Integral and Singularity Methods for Linearized Viscous Flow. Cambridge University Press, Cambridge, UK (1992)

Reddy, J.N., Gartling, D.K.: The Finite Element Method in Heat Transfer and Fluid Dynamics. pp. 149–185. CRC Press, USA (2001)

Roberts, A.P.: Statistical reconstruction of three-dimensional porous media from two-dimensional images. Phys. Rev. E **56**(3), 3203–3212 (1997)

Sahimi, M., Heiba, A., Scriven, L., Davis, H.: Dispersion in flow through porous media-I. One phase flow. Chem. Eng. Sci. **41**(8), 2103–2122 (1986)

Soll, W.E., Celia, M.A., Wilson, J.L.: Micro-model studies of three fluid porous media systems: pore-scale processes relating to capillary pressure saturation relationships. Water Resour. Res. **29**(9), 2963–2974 (1993)

Spanne, P., Thovert, J.F., Jacquin, C.J., Lindquist, W.B., Jones, K.W., Adler, P.M.: Synchrotron computed microtomography of porous media—topology and transports. Phys. Rev. Lett. **73**(14), 2001–2004 (1994)

Talabi, O., Alsayari, S., Blunt, M.J., Dong, H., Zhao, X.: Predictive pore-scale modeling: from three-dimensional images to multiphase flow simulations. In: Proceedings of the Society of Petroleum Engineers, Denver, SPE 115535, 2008

Tsay, R.Y., Wienbaum, S.: Viscous flow in a channel with periodic cross-bridging fibers: exact solutions and Brinkman approximation. J. Fluid Mech. **226**, 125–148 (1991)

Valvatne, P.H., Blunt M.J.: Predictive pore-scale modeling of two-phase flow in mixed wet media. Water Resour. Res. **40**, W07406 (2004). doi:10.1029/2003WR002627

van-Genuchten, M.T.: A closed-form equation for predicting the hydraulic conductivity of unsaturated soils. Soil Sci. Soc. Am. J. **44**, 892–898 (1980)

Wildenschild, D., Hopmans, J.W., Rivers, M.L., Kent, A.J.R.: Quantitative analysis of flow processes in a sand using synchrotron-based X-ray microtomography. Vadose Zone J. **4**, 112–126 (2005)

Yen, M.R.T., Fung, Y.C.: Model experiments on apparent blood viscosity and hematocrit in pulmonary alveoli. J. Appl. Physiol. **35**, 510–517 (1973)

Zimmerman, R.W., Bodvarsson, G.S.: Hydraulic conductivity of rock fractures. Transp. Porous Media **23**, 1–30 (1996)

Zimmerman, R.W., Kumar, S.: A fluid-mechanical model for blood flow in lung alveoli. HTD-Vol. 189/BED-Vol. 18, Advances in Biological Heat and Mass Transfer, ASME, 1991